Atmospheric Environment 246 (2021) 118102

Contents lists available at ScienceDirect

Atmospheric Environment

journal homepage: http://www.elsevier.com/locate/atmosenv

Short communication

Remote sensing of a high-Arctic, local dust event over Lake Hazen (Ellesmere Island, Nunavut, Canada)

Keyvan Ranjbar [a,*], Norm T. O'Neill [a], Liviu Ivanescu [a], James King [b], Patrick L. Hayes [c]

[a] Centre d'Applications et de Recherches en Télédétection, Université de Sherbrooke, Sherbrooke, Québec, Canada
[b] Département de Géographie, Université de Montréal, Montréal, Québec, Canada
[c] Département de Chimie, Université de Montréal, Montréal, Québec, Canada

HIGHLIGHTS

- A springtime, high-Arctic dust plume over Lake Hazen, Nunavut, Canada was detected using satellitebased remote sensing.
- This is likely the first remotely sensed overland capture of a local dust plume over the Arctic.
- Arctic-adapted RS techniques incorporating dust optical properties can be exploited to investigatelocally generated plumes.

ARTICLE INFO

Keywords:
Local dust plume
Arctic-adapted remote sensing techniques for dust detection
Dust optical properties
Drainage wind
High Arctic
Lake Hazen

ABSTRACT

A dust plume rising to a maximum altitude of about 1 km above the springtime high-Arctic terrain of Lake Hazen, Nunavut, Canada was detected using a diverse array of passive and active, satellite-based remote sensing techniques. We were able to broadly characterize the 532 nm optical depth and particle size of the upper plume (0.5 ± 0.2 and 15–25 μm radius limits respectively). To our knowledge this is the first satellite-based remotely sensed, overland capture of what is an ubiquitous aeolian process across the Arctic: drainage winds inducing dust plumes that are funneled along basin pathways to spread over the water and land surfaces at the outlets of those pathways. The identification and characterization of the Lake Hazen plume was challenging given that there is little development of passive and active remote sensing techniques over Arctic terrains. Our findings suggest that Arctic-adapted remote sensing techniques that incorporate a priori information on dust optical properties can be exploited to identify and characterize locally generated plumes.

1. Introduction

Mineral aerosols constitute the largest uncertainty of global radiative forcing. This derives from uncertainties in their direct and indirect effects as well as in their frequency and magnitude (Boucher et al., 2013). Direct radiative impacts are responsible for up to 250 Wm^{-2} of surface insolation, while indirect feedbacks such as cloud production or suppression are equally important (Lohmann and Feichter, 2005; Tang et al., 2016). Additionally, mineral aerosols (MA) transport minor and trace elements important to ecological functions. MA also decrease air quality: this has health impacts on wildlife as well as in populated regions (Karanasiou et al., 2012).

Within arid regions, fugitive emissions of MA are the result of the availability of dust-sized material on the surface coupled with wind speeds that exceed the particle entrainment threshold. In most of these regions, erodible particles are always available or are renewed regularly by fluvial events and subsequently liberate dust-sized particles through a saltation bombardment process (Shao et al., 1993). Wind events demonstrate synoptic, regional or jet-like characteristics with their relative importance being dependent on the geographical region. However, there is a growing recognition of the importance of jet-like flows (e.g., nocturnal low-level jet) for generating emissions (Washington and Todd, 2005) inasmuch as their high frequency relative to synoptic scale generated winds, are not transport capacity dependent (Allen et al., 2013). Drainage flows (which include katabatic flows) are a sub-class of jet-like flows: they are generated in mountainous regions and have diurnal frequencies with extremely high near-surface winds independent of synoptic systems. Winds generated by these flows drive

* Corresponding author.
E-mail address: keyvan.ranjbar@usherbrooke.ca (K. Ranjbar).

https://doi.org/10.1016/j.atmosenv.2020.118102
Received 1 June 2020; Received in revised form 7 October 2020; Accepted 23 November 2020
Available online 27 November 2020

emissions of high latitude MA (HLMA). They are influenced by mountain topography and large temperature contrasts: more regional or synoptic components cannot develop enough energy.

HLMA have recently been identified as a potentially strong influence on climate (Bullard et al., 2016). These influences exceed (per unit mass), those of MA that are produced, transported, and deposited at lower latitudes. This is ascribed to the high likelihood of HLMA (depositing on snow, ice and frozen bare ground) increasing snow or ice ablation rates as well as the increased effects of nutrient deposition (e.g., Fe, P) within a highly disconnected and nutrient limited landscape and the attendant increase in terrestrial and aquatic productivity (Schroth et al., 2017). Furthermore, with the influence of anthropogenic climate change being enhanced in polar regions (Lehnherr et al., 2018), it is hypothesized that the number and frequency of emissions of Arctic-based MA could increase as snow and ice coverage decrease, summer seasons elongate, and precipitation patterns change (Bullard et al., 2016).

Despite the potential for HLMA playing an important global-climate role, their geographical identification, frequency, and intensity, outside of several well-monitored research areas, are not well known. Those that have been identified and researched include several sources in Iceland (Baddock et al., 2017; Prospero et al., 2012) and Greenland (Bullard and Mockford, 2018). Distinct sources within North America include the Copper River, Alaska (Crusius et al., 2011), Kluane Lake, Yukon (Bachelder et al., 2020), and southern Baffin Island, Nunavut (Neuman, 1990). With the identification of other HLMA sources (from World Meteorological Organization weather codes for blowing dust as per Engelstaedter et al., 2003), it is suggested that between 3% and 5% of the global dust budget (Bullard et al., 2016) or around 5–10 Mt originates from high latitudes (Zwaaftink et al., 2016). With a sparse monitoring network and known seasonality of small-area source regions (hindering the ability to identify and quantify contributions), this likely underestimates the ratio of HLMA to global mineral aerosol emissions.

Remote sensing images acquired using passive sensors aboard various satellite platforms enhance our ability to identify and characterize aerosol-plume events using multi-spectral (e.g., MODIS, VIIRS, Aerosol Index images produced by OMI) and multi-angle (e.g., MISR and PARASOL) techniques while active sensors (notably the CALIOP lidar) provide vertical profile and some speciation capabilities to support the identification and characterization of aerosol events. There are numerous examples in the literature on the active and passive remote sensing of wind-eroded desert dust plumes at southern latitudes (see, for example, Xie et al., 2017 and Hsu et al., 2013 for remote sensing investigations over the Chinese and Saharan desert and Huang et al., 2008 and Peyridieu et al., 2013 for investigations of dust plumes over the Pacific and Atlantic Ocean). To date, the capture of HLMA events using remote sensing techniques has, however, been largely limited to plumes over water (see for example, Crusius et al. (2011) for an event captured using MODIS visible imagery over the Gulf of Alaska). There is substantial remote sensing literature on the inference of mid-latitude dust transport and subsequent dust deposition effects derived from changes in the surface reflectance of snow or ice in mountainous regions (see, for example Painter et al., 2012; Seidel et al., 2016).

Optimized as they are for low altitude conditions, the products of aerosol remote sensing sensors are often not attuned to the unusual conditions such as those found in the Arctic. In this study we demonstrate how the multi-dimensional information content of four sensors (MODIS, MISR, CALIOP and CloudSat) was exploited and readapted to identify a singular springtime (May) plume event over Lake Hazen, Nunavut in the Canadian high Arctic.

2. Relevant site information

2.1. Lake Hazen

Lake Hazen is located on Ellesmere Island in the territory of Nunavut, Canada. It extends from about 81.7°N 73.0°W to 81.9°N 68.9°W and is the Arctic's largest lake, by volume (51.4 km^3). Fig. 1 delineates the Lake Hazen watershed, the different glaciers in that watershed as well as the glacial rivers associated with the sub-watersheds of each glacier. Lake Hazen camp (also known as Hazen base camp), is indicated on the north shore of the lake.

2.2. Brief climatology of Lake Hazen

Hudson et al. (2001) present a climatological overview of Nunavut and Arctic weather with a brief section on Lake Hazen. The Lake Hazen watershed is classified as a semi-polar desert and is known as a high Arctic "thermal oasis" (St Pierre, 2018). Jackson (1960) underscored the generally unique calmness of Lake Hazen in contrast to a coastal site such as Alert (~150 km to the northeast of Lake Hazen camp). No nearby in situ meteorological observations are available during the period of the dust event described in this paper. We did, however, find a five-year climatic data set for Lake Hazen camp (2008–2012) that we have included in the Data Set S1. The temperature statistics for the month of May (computed from the ensemble of daily averages during this 5-year period), show an average temperature of -3.8 ± 3.0 °C with a 0 °C crossing typically occurring in early June.

There are few temperature radiosondes over Lake Hazen reported in the published and unpublished literature. Figure S2 shows four vertical profiles acquired along a rare April 10, 2015 flight from Alert to Eureka (about 330 km southwest of Lake Hazen camp): an ascent from Alert, a descent from Lake Hazen, an ascent from Tanquary Fjord and a relatively tight spiral descent to Eureka (see flight trajectory in Figure S1). One can see boundary layer temperature inversions for the Alert and Eureka flight segments while the Lake Hazen and Tanquary Fjord segments show no inversions. The less sheltered sites of Alert and Eureka are apparently subject to the more regional and strong Arctic inversions characteristic of the polar winter and spring (Bradley et al., 1993) while the more sheltered Lake Hazen and Tanquary Fjord profiles are not incoherent with Jackson (1965) inference of a shallow summertime inversion layer over Lake Hazen (and by extension a progressive transformation from a strong polar winter inversion to less extreme inversion conditions during the late spring and summer).

2.3. Drainage winds over Lake Hazen

Our analysis of the 2008 to 2012 wind speed data showed a high degree of variability and a year to year increasing trend that was difficult to justify given the available supporting information. We chose instead to use an older 12-year (1988–1999) Lake Hazen climate data set that showed a more consistent year to year variability (see Data Set S2). The ensemble of daily wind velocity results for the 12 year Lake Hazen archive (see Fig. 2) indicates the predominance of calm winds for the majority of time with distinct high wind events likely associated with topographically induced drainage (Jackson, 1960). Previous research has determined daily windspeed thresholds for emissions to range from 4 to 7 $m\text{-}s^{-1}$ depending on the soil conditions (Stout, 2001; Whicker et al., 2002). The ensemble wind velocity results for the 12-year Lake Hazen archive shows that during the month of May, daily wind speeds greater than 4 and 7 $m\text{-}s^{-1}$ occurred 6.5 and 4.0% of the time, respectively.

3. Remote Sensing tools

3.1. MISR

MISR, aboard the Terra satellite, provides near simultaneous observations at nine viewing angles in three VIS and one NIR band (see Figure S3, for details concerning those viewing angles). MISR has a much narrower swath width than the MODIS imager (380 km versus 2330 km) with a resampled spatial resolution of 275 m. Stereoscopic

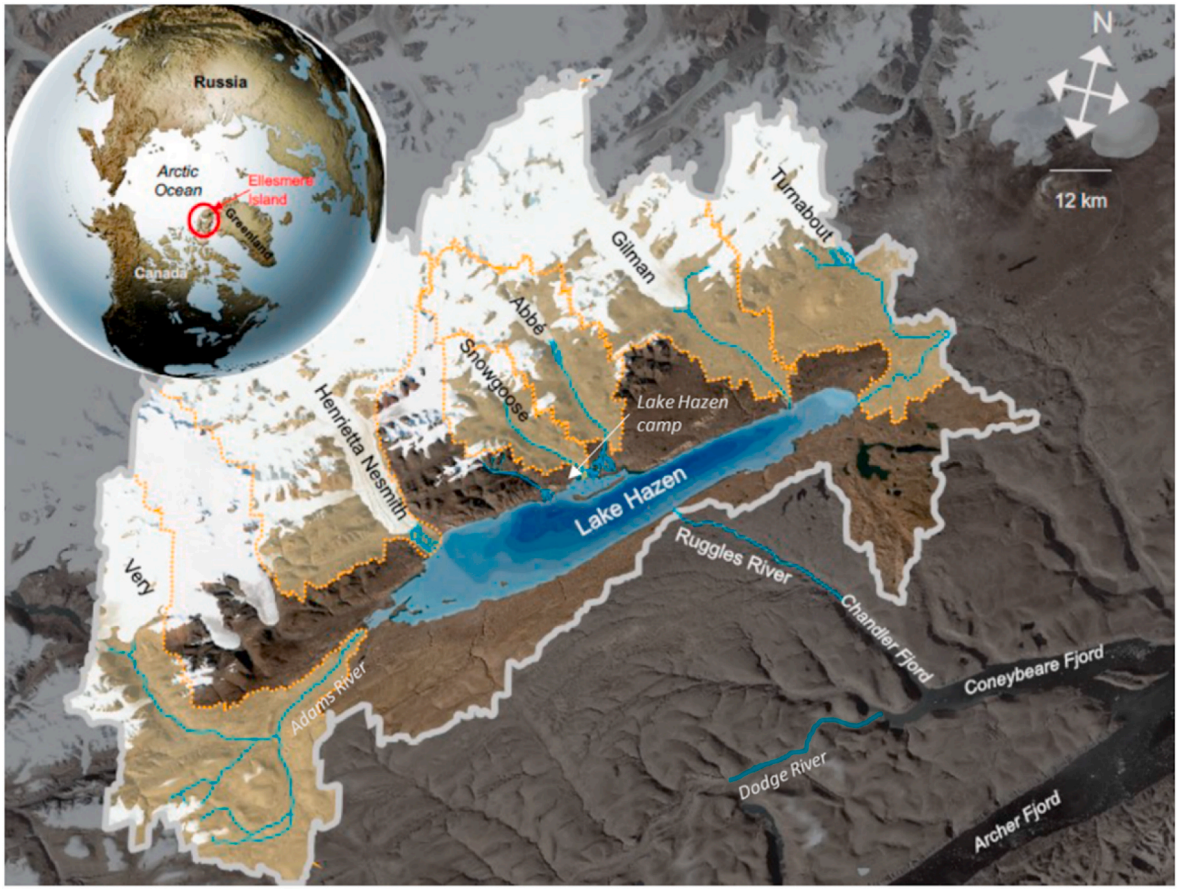

Fig. 1. Map of the Lake Hazen watershed (grey outline) on northern Ellesmere Island (see inset map). Major hydrologic features as well as associated glaciers are identified (sub-watersheds are delineated in orange). Important Lake Hazen glacial rivers are shown in cyan (as well as Dodge River feeding into Coneybeare Fjord). Adapted from St Pierre (2018). (For interpretation of the references to colour in this figure legend, the reader is referred to the Web version of this article.)

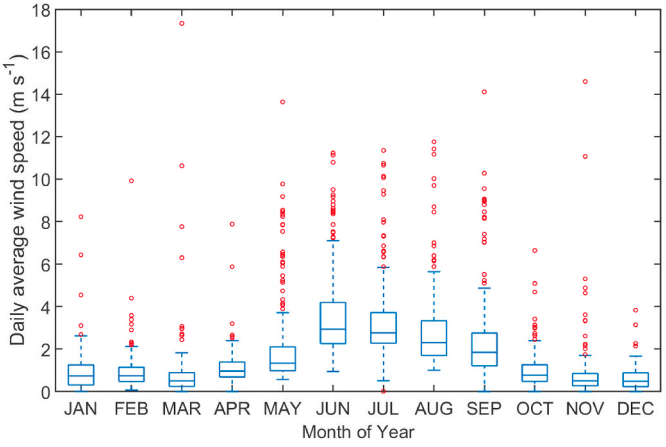

Fig. 2. Box-and-whisker plot of daily average wind speed as a function of month of the year for the ensemble of the 12-year (1988–1999) Lake Hazen meteorological data set.

techniques applied to co-registered layers of the different angular views enables construction of 3-D models that yield images of aerosol or cloud plume height as well as the horizontal velocities of matching plume pixels. At the same time, the contextual capability of visually confirming the movement of unique portions of a plume is a means of adding confidence to the automated matching exercise of extracting plume altitude and speed.

3.2. MODIS

The MODIS imagers aboard the Terra and Aqua satellites acquire UV to thermal-IR imagery in 36 bands across a 2330 km swath at a spatial resolution varying from 250 to 1000 m. The fact that MISR and MODIS-Terra share the same Terra platform provides simultaneous observations which synergize their remotely sensed information content. The broad spectral range of MODIS imagery enables the extraction of aerosol/cloud information that complements the MISR retrieval products. However, snow/ice surfaces and low solar zenith angles complicate aerosol, solar-reflective retrievals over the Arctic (see, for example, Mei et al., 2013).

A dust remote sensing approach with a longer heritage than solar reflective techniques is the BTD technique involving pairs of TIR (thermal IR) bands (see, for example, Miller et al. (2017) for an overview of different BTD techniques). A BT, sensitive to higher altitude plume absorption and/or scattering interactions in a given TIR band is subtracted from a BT reference that is highly transmitting and more sensitive to the surface BT. Ackerman (1997) presented two robust BTD indicators that could be employed for dust discrimination in the presence of competing signals such as clouds, sea surface and different types of desert surfaces. From dust-free (background) parts of a scene to regions of thick dust, the two BTDs employed ($BT_{8.5} - BT_{11}$ and $BT_{11} - BT_{12}$) showed a tendency, respectively, for large negative values tending toward small positive values and positive values leading towards small negative values (where the subscripts "8.5", "11" and "12" refer to approximate band centers in μm of MODIS bands 29, 31 and 32 respectively). These BTD techniques were, however, generally limited to warm desert scenes: their extension to the detection of a dust plume over a heterogeneous high-Arctic surface is discussed below.

3.3. CALIOP and CloudSat

The CALIOP aerosol/cloud lidar aboard the CALIPSO satellite produces two dimensional "curtains" of 532 nm backscatter profiles along a polar-orbit track. The cloud profiling radar aboard the CloudSat satellite produces analogous backscatter curtains in the same (A-train) polar orbit (MODIS-Aqua, CALIOP and CloudSat were all members of the A-train at the time of this event; CALIOP and CloudSat have recently been moved to a lower orbit). The 3D cross section perspective from the intersection of CloudSat/CALIOP profiles and MODIS-Aqua imagery as well as MISR multi-angle imagery and MODIS-Terra imagery provides a valuable spatial contextualization tool for identifying and understanding particulate backscatter events. An overview description of CALIOP and its processing algorithms can be found in Winker et al. (2009). A similar document for CloudSat can be found in Stephens et al. (2008).

3.4. General comments

The polar orbits of the CALIOP, CloudSat, MISR and MODIS platforms enable a much larger satellite product density in time and space at high latitudes as compared to more southern sites. This largely ensures the identification of any optically significant aerosol event on any given day (cloud cover being virtually the only constraint in at least visually identifying such an event).

4. Local dust event description

Movie S1 shows a video of the dust storm made by a ground party at Lake Hazen camp on the morning of May 20, 2014 while Figure S4 shows photos taken before and after the dust event (May 16 and May 20, 2014 respectively). The latter photo was taken at 16:02 local time (EDT or hence 12:02 UT): the general calm nature of the scene captured by the photo relative to the severe conditions evident in the morning video indicates that the dust storm ended rather abruptly.

4.1. Identification of the dust plume

Fig. 3a shows a true-colour georeferenced, RGB MODIS-Terra image acquired on May 19, 2014 at 15:50 EDT (19:50 UT) clipped to the area of Fig. 1. One can distinguish glaciers and snow/ice covered terrain, what appears to be a mostly ice/snow covered Lake Hazen, dust on the ground about and on the lake as well as the Adams River Valley and, as we argue below, a distinct dust plume. One can also make analogous surface-dust affirmations in the region of the Dodge River and other tributaries. The blue broken-line square at the bottom of Fig. 3a shows a zoom of a conical structure that we believe to be a dust plume. In this section we try to validate this visual affirmation.

Figure S5 incorporates an animation of the 9 MISR true-colour images acquired by the 9 forward to aft cameras. It shows the conical structure of Fig. 3a apparently emanating from the Adams River Valley and moving in a northeast direction. We would expect this movement to be observable given the eye's capability of following the coherent motion of complex objects: the apparent velocity of the plume (core velocities of $<\sim$10 m-s^{-1} as discussed below) and the 7 min needed to acquire the 9 MISR Lake Hazen images (Nelson et al., 2013) means that the plume will have moved $<\sim$4.2 km or $<\sim$15 MISR pixels during that 7 min period.

The implementation of the desert dust BTD methodology discussed above to the high Arctic case of the Lake Hazen plume also needs justification. Aside from the large changes in temperature magnitudes from a desert to a high Arctic environment we have argued above for a Lake Hazen thermal environment that does not include a temperature inversion (or at least not a strong temperature inversion). Figure S6 also suggests that such a thermal lapse rate existed on May 19, 2014: the superposition of the MODIS BT_{11} (high transmission, reference) image on the MISR-generated elevation model generally supports the absence of an inversion layer. Ackerman's BTD development included the reference to the background desert aerosol (fine mode aerosols with a radius peak $\sim$ 0.1 μm and very small single-scattering albedo values (strong absorption) around 8.5 μm). Such a background aerosol is quite similar to ubiquitous Arctic haze aerosols in general: Ritter et al. (2005), for example, measured significant TIR optical depth values (at the high

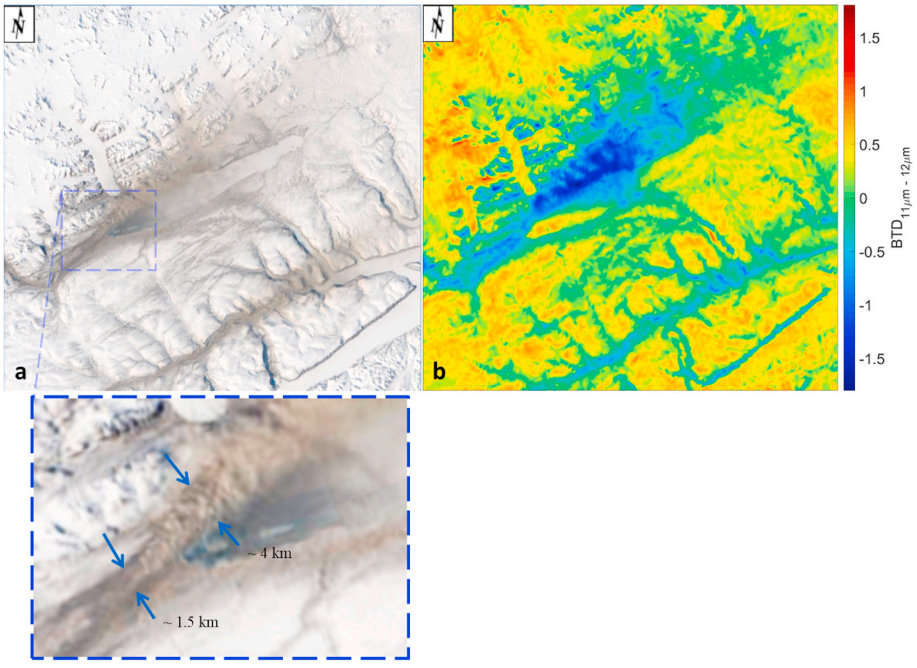

Fig. 3. MODIS-Terra May 19, 2014, 19:50 UTC (a) true-colour image. (b) BTD = $BT_{11} - BT_{12}$. The true colour image: MODIS channels 1 (620–670 nm), 3 (459–479 nm) and 4 (545–565 nm) are, respectively, loaded into the RGB channels of the display. (For interpretation of the references to colour in this figure legend, the reader is referred to the Web version of this article.)

Arctic site of Ny Alesund) which they attributed to the strongly absorbing nature of sulfate aerosols in the TIR. Vincent (2018) makes the most compelling combination of theoretical and empirical case for $BT_{11}-BT_{12}$ dust sensitivity in the Arctic. He contends that the increase in dust emissivity from the 11–12 μm MODIS bands is responsible for the uniquely negative $BT_{11}-BT_{12}$ signature of dust and suggests that the ubiquitous multi-year observation of that signature over ice and open-water MODIS scenes of the Amundsen Gulf region is due to Asian and possibly local dust (whether that dust is airborne or deposited on the surface).

Fig. 3b shows the BTD ($BT_{11}-BT_{12}$) image corresponding to the MODIS RGB image of Fig. 3a. A clear (negative) minimum in the neighborhood of the thickest portion of the RGB plume can be observed. To better understand the interdynamics between the BT images relative to the RGB image the reader can consult Figure S7. A similar degree of (positive) plume discrimination was observed for the $BT_{8.5}-BT_{11}$ image (the same sequence of alternating images is shown in Figure S8).

4.2. Plume height and speed

Fig. 4 shows the wind-corrected plume height (km ASL) superimposed on the MISR RGB, nadir image. The largest and most dense collection of plume height retrievals correspond well with the thick Adams River plume that was visually and thermally identified in the previous section. Fig. 5a shows the corresponding MISR-derived, zero-wind heights, wind-corrected heights, and terrain height for pixels along the 12:06 UT CALIOP orbit line (the purple broken line of Fig. 4). Fig. 5b shows the CALIOP 532 nm total attenuated backscatter profile. The high values of total attenuated backscatter coefficient outlined by the two yellow rectangles are in about the same position and height along the CALIOP orbit line as the two height peaks of the MISR profile. We presume that the fact that CALIOP does not show an obvious return over Lake Hazen (where MISR appears to detect a 3rd lower plume) is due to the nearly 8 h of difference in the acquisition of the MISR image and the CALIOP profile (see the Fig. 5 caption).

An image of MISR-derived total wind speed is shown in Figure S9. While that image does show maximum values for the Adams River plume, they are not inordinately large (<~10 m-s^{-1}). However, as indicated above, the speed of drainage flows are typically known to decrease significantly with increasing altitude (see Renfrew and Anderson, 2006 for example). NOAA reanalysis data (2.5° grid cells) indicated a general increase in regional wind speeds in the northern half of Ellesmere Island (Lake Hazen, and Alert) rising from about 6 m-s^{-1} at 00:00 19 May to around 13 m-s^{-1} at 12:00 19 May (c.f. Data Set S3). This increase suggests a link between the reanalyzed wind fields and the low level MISR-derived drainage flow wind speeds. The general direction of the plume flow in Fig. 3 at the MODIS-Terra time of 12:06 UT was approximately 42° clockwise (CW) from north while the reanalysis wind direction near the MODIS-Terra time was about 23° CW from north (c.f. Data Set S3).

4.3. Characterization of dust properties

The MODIS aerosol optical depth retrieval process failed to detect aerosols (let alone dust aerosols): the vast majority of pixels were classified as clouds. Similarly, the vast majority of plume pixels were classified as clouds by the CALIOP classification process (Figure S10). The combined CALIOP/CloudSat ice cloud classification process does not include an aerosol classification product (c.f. Figure S11). The DARDAR (CALIOP, CloudSat, CALIPSO IR imager) classification product (DARDAR-MASK) includes aerosol classification but no pixels were classified as aerosols (Figure S12).

In order to at least obtain order of magnitude estimates of optical depth ($\Delta\tau$) and effective particle radius (r_{eff}) of the upper plume (defined generally by the highest S/N part of the plume in Fig. 4b and more specifically in the caption of Table 1 of Text S1) we employed the DARDAR retrievals as a baseline from which uncertainties could be calculated from an extreme interpretation of the uncertainty in r_{eff} and $\Delta\tau$ estimates: we applied what is arguably an excess of caution in imagining that the intrinsic optical/microwave parameters must lie

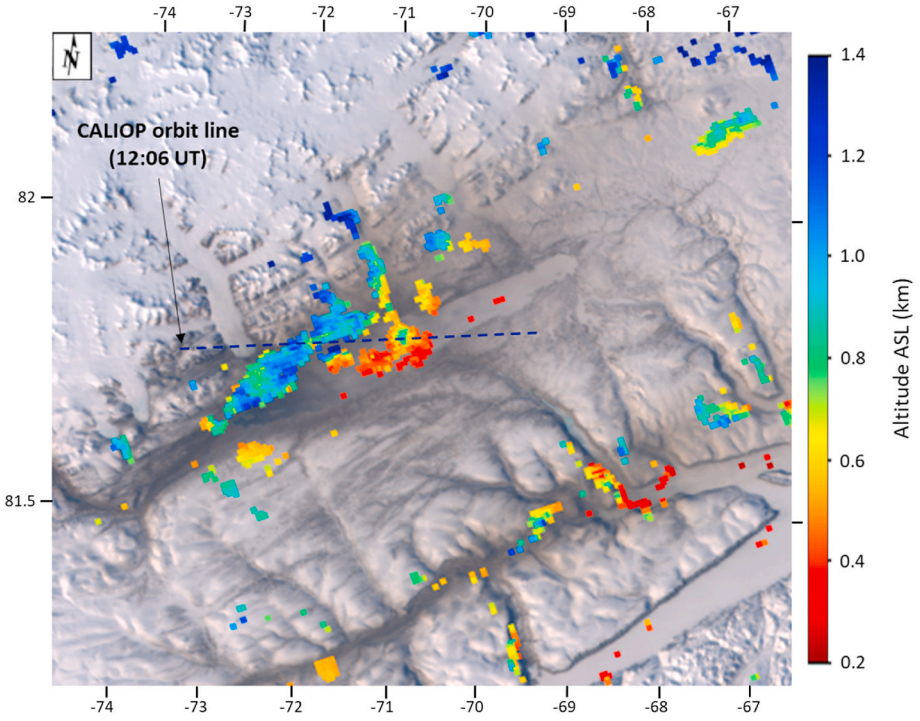

Fig. 4. May 19, 2014, MISR wind-corrected heights superimposed on the MISR RGB, nadir image (algorithmic details are given in Text S2). The heights are represented by a red to blue colour scale (using a colour-activation threshold of 200 m). The purple dashed line shows the orbit line of the Fig. 4b (CALIOP) altitude profile. Latitude and longitude coordinates, in degrees are shown on x and y axes.

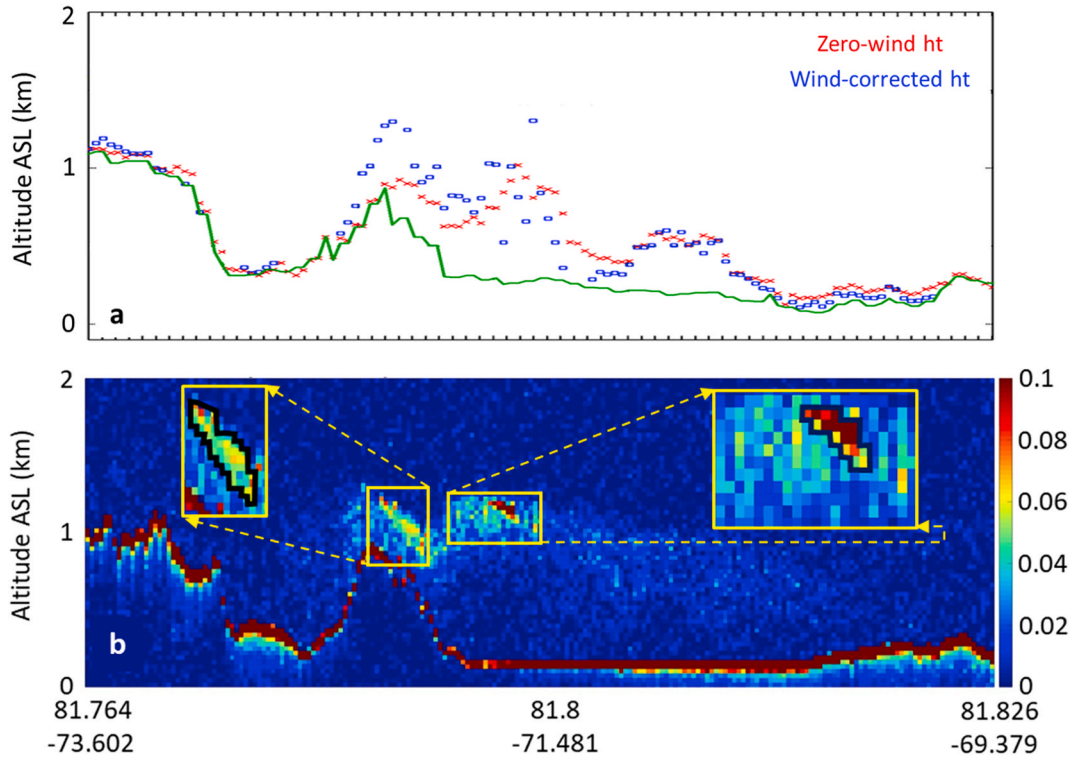

Fig. 5. (a) MISR plume height and (b) CALIOP total attenuated backscatter coefficient (km^{-1} sr^{-1}). The MISR profile corresponds to the height information of Fig. 4 where the heights are constrained to pixels along the purple-dashed (CALIOP) orbit line. The CALIOP profile was acquired on May 19, 2014, 12:06 UT (about 7 h and 40 min before the MISR overpass). Details on the CALIOP profile can be found in the Figure S10 caption. (For interpretation of the references to colour in this figure legend, the reader is referred to the Web version of this article.)

somewhere between the extreme limits of pure dust and pure ice-cloud plumes: from the latter values of r_{eff} and $\Delta\tau$ we estimate the means between pure dust and pure ice-cloud and their associated uncertainty (see more details in Text S1). This yielded a 532 nm $\Delta\tau$ estimate of 0.5 ± 0.2 and broad r_{eff} limits of 15–87 μm for upper plume particles. An additional constraint on the r_{eff} upper limit is provided by the average distance taken for local dust particles to fall out of a local dust plume: Bullard (2013) places an upper limit of ~25 μm radius on glacigenic dust particles that have travelled beyond 10 km (the approximate distance between the apparent source and the position of the Fig. 5 upper plume): this defines more workable r_{eff} bounds between ~ 15 and 25 μm.

5. Conclusions

A high Arctic dust plume over the complex ice, snow and dust embedded terrain of the Lake Hazen, Nunavut watershed was detected using a diverse array of passive and active, satellite-based remote sensing techniques. In addition we were able to broadly characterize the 532 nm optical depth and particle size of the upper plume (0.5 ± 0.2 and 15–25 μm radius limits respectively). Dust particles of radius beyond the upper radius bound are largely limited to transport distances <~10 km.

To our knowledge this is the first such remotely sensed, satellite-based overland capture of what is a ubiquitous aeolian process across the Arctic: drainage winds inducing dust plumes that are funnelled along basin pathways to spread over the water and land surfaces at the outlets of those pathways. The identification and characterization of the Lake Hazen plume was challenging given that there is little development of passive and active remote sensing techniques over Arctic terrains and that these techniques, as well as active techniques (CALIOP and CloudSat) failed to identify a dust component in the plume. We note that Dörnbrack et al. (2010) reported on the airborne-lidar capture of a local dust plume over a Svalbard Fjord in May of 2004 while Vincent (2018) reported on robustly negative BT_{11}– BT_{12} signatures over snow/ice as well as open-water MODIS scenes in the Amundsen Gulf region that he attributed to Asian dust. Mei et al. (2020), using AATSR imagery and their XBAER algorithm, retrieved continent-wide coarse mode (super micron) optical depths over Greenland ice/snow imagery on April 9, 2011 that they attributed to long range transport of African dust.

The apparent effects of dust deposition and/or dust entrainment along the Adams River Valley appears as springtime browning over 20 years of MODIS true-colour imagery in the Lake Hazen region (Movie S2). Woo et al. (1991) observed snow-melt zones on the Fosheim Peninsula (the location of Eureka) that corresponded to “dark spots” on a map derived from NOAA imagery (AVHRR 1 km resolution imagery acquired on May 17, 1990). They noted that the first area to experience significant snow melt in their map zone was dust covered. We found what appeared to be snow-free and/or dust covered watershed patterns in MODIS imagery to be readily observable as dark/brownish features across Ellesmere Island on the day of our dust event (see Figure S13 for Fosheim Penninsula and Lake Hazen illustrations in the northern part of Ellesmere Island). In particular, the Fosheim Penninsula imagery when clipped to the dimensions of Woo et al.’s AVHRR-derived map (Fig. 6a) shows rather remarkable spatial correlation with their “shaded” (dotted) regions derived from their AVHRR imagery some 24 years earlier. Ground teams had ascertained (about the regions marked “E”, “H” and “U”) that shaded regions were snow free and that unshaded regions were snow covered.

A hypothesis that the darkening/browning of snow or ice covered Arctic surfaces is largely the result of wind blown dust deposition suggests a means of searching for potential dust plumes by employing reflectance changes in the basin pathways as flags for their presence. One could then focus passive and active remote sensing techniques (multi-angle imagery, satellite-based lidar and radar profiles, BTD imagery, etc) near the outlets or along the basin pathways to search for plumes. This systematic identification and subsequent characterization of dust plumes would be valuable in better understanding the driving

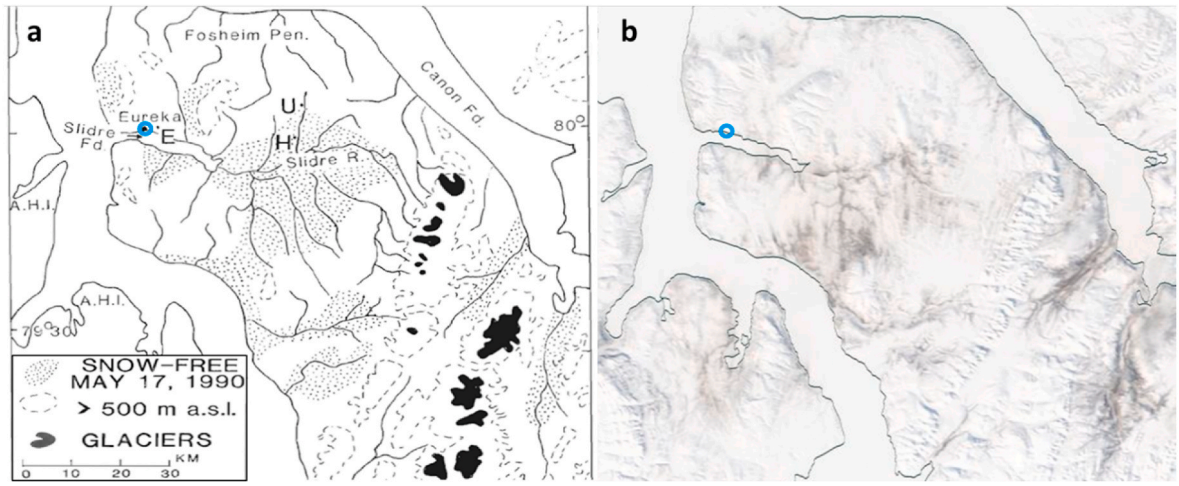

Fig. 6. (a) Fig. 1 of Woo et al., (1991) (b) Fosheim Penninsula sub-image of Figure S13. Note the correspondence between the "snow-free" (dotted) areas of Woo et al. and the dark/brownish regions of the MODIS sub-image.

mechanisms that generate the apparent dust covered snow/ice surfaces along watershed pathways.

The comprehensive review of Bullard et al. (2016) on the importance of high latitude dust to the earth system underscored the limitations of remotely sensed information as a means of monitoring locally generated high latitude dust. Our findings suggest that remote sensing retrieval techniques, adapted to the special conditions of the Arctic landscape and incorporating a priori information on dust optical properties can be better exploited to first flag and then investigate locally generated dust plumes over the large expanses of Arctic area where there can be no practical aspirations of deploying dedicated sites or measurement campaigns. This approach must necessarily take full advantage of the newest and upcoming generation of aerosol- and cloud-dedicated, multi-dimensional sensors (TROPOMI and VIIRS, the Aeolus Doppler lidar, the EarthCare ATLID lidar and CPR radar, the A-CCP missions, etc.).

CRediT authorship contribution statement

Keyvan Ranjbar: Writing - original draft, Visualization, Investigation, Formal analysis, Conceptualization, Methodology, Data curation, Software. **Norm T. O'Neill:** Writing - original draft, Writing - review & editing, Visualization, Investigation, Supervision, Methodology, Validation, Funding acquisition, Formal analysis. **Liviu Ivanescu:** Writing - review & editing, Formal analysis, Resources. **James King:** Writing - original draft, Writing - review & editing, Formal analysis. **Patrick L. Hayes:** Writing - review & editing, Formal analysis.

Declaration of competing interest

The authors declare that they have no known competing financial interests or personal relationships that could have appeared to influence the work reported in this paper.

Acknowledgements

We gratefully acknowledge funding from the PAHA project (NSERC-CCAR program; RGPCC-433842-2012), the SACIA project (CSA-ESSDA program; 16UASACIA), the CMN (NCE program; RES0044975) and the NSERC DG grants of Hayes, King and O'Neill (RGPIN-2017-05531, RGPIN-2016-05417 and RGPIN-05002-2014). We also gratefully acknowledge usage of data from the following sites; https://eosweb.larc.nasa.gov/project/calipso/calipsotable (CALIOP data), http://www.cloudsat.cira.colostate.edu/order-data (CloudSat data), icare.univ-lille1.fr/projects/dardar" title = "http://www.icare.univ-lille1.fr/projects/dardar">http://www.icare.univ-lille1.fr/projects/dardar (DARDAR data), https://ladsweb.modaps.eosdis.nasa.gov/search/(MODIS data), https://l0dup05.larc.nasa.gov/MISR/cgi-bin/MISR/main.cgi (MISR data), https://psl.noaa.gov/data/composites/hour/(reanalysis data) and https://climate.weather.gc.ca/historical_data/search_historic_data_e.html (weather data).

Appendix A. Supplementary data

Supplementary data related to this article can be found at https://doi.org/10.1016/j.atmosenv.2020.118102.

References

Ackerman, S.A., 1997. Remote sensing aerosols using satellite infrared observations. J. Geophys. Res. Atmos. 102, 17069–17079.
Allen, C.J.T., Washington, R., Engelstaedter, S., 2013. Dust emission and transport mechanisms in the central Sahara: fennec ground-based observations from Bordj Badji Mokhtar, June 2011. J. Geophys. Res. Atmos. 118, 6212–6232.
Bachelder, J., Cadieux, M., Liu-Kang, C., Lambert, P., Filoche, A., Galhardi, J.A., Hadioui, M., Chaput, A., Bastien-Thibault, M.-P., Wilkinson, K.J., King, J., Hayes, P. L., 2020. Chemical and microphysical properties of wind-blown dust near an actively retreating glacier in Yukon, Canada. Aerosol Sci. Technol. 54, 2–20.
Baddock, M.C., Mockford, T., Bullard, J.E., Thorsteinsson, T., 2017. Pathways of high-latitude dust in the north atlantic. Earth Planet Sci. Lett. 459, 170–182.
Boucher, O., Randall, D., Artaxo, P., Bretherton, C., Feingold, G., Forster, P., Kerminen, V.-M., Kondo, Y., Liao, H., Lohmann, U., 2013. Clouds and aerosols. In: Climate Change 2013: the Physical Science Basis. Contribution of Working Group I to the Fifth Assessment Report of the Intergovernmental Panel on Climate Change. Cambridge University Press, pp. 571–657.
Bradley, R.S., Keimig, F.T., Diaz, H.F., 1993. Recent changes in the North American Arctic boundary layer in winter. J. Geophys. Res. Atmos. 98, 8851–8858.
Bullard, J.E., 2013. Contemporary glacigenic inputs to the dust cycle. Earth Surf. Process. Landforms 38, 71–89.
Bullard, J.E., Baddock, M., Bradwell, T., Crusius, J., Darlington, E., Gaiero, D., Gasso, S., Gisladottir, G., Hodgkins, R., McCulloch, R., 2016. High-latitude dust in the Earth system. Rev. Geophys. 54, 447–485.
Bullard, J.E., Mockford, T., 2018. Seasonal and decadal variability of dust observations in the Kangerlussuaq area, west Greenland. Arctic Antarct. Alpine Res. 50, S100011.
Crusius, J., Schroth, A.W., Gasso, S., Moy, C.M., Levy, R.C., Gatica, M., 2011. Glacial flour dust storms in the Gulf of Alaska: hydrologic and meteorological controls and their importance as a source of bioavailable iron. Geophys. Res. Lett. 38.
Dörnbrack, A., Stachlewska, I.S., Ritter, C., Neuber, R., 2010. Aerosol distribution around Svalbard during intense easterly winds. Atmos. Chem. Phys. 10, 1473–1490.
Engelstaedter, S., Kohfeld, K.E., Tegen, I., Harrison, S.P., 2003. Controls of dust emissions by vegetation and topographic depressions: an evaluation using dust storm frequency data. Geophys. Res. Lett. 30.
Hsu, N.C., Jeong, M., Bettenhausen, C., Sayer, A.M., Hansell, R., Seftor, C.S., Huang, J., Tsay, S., 2013. Enhanced Deep Blue aerosol retrieval algorithm: the second generation. J. Geophys. Res. Atmos. 118, 9296–9315.
Huang, J., Minnis, P., Chen, B., Huang, Z., Liu, Z., Zhao, Q., Yi, Y., Ayers, J.K., 2008. Long-range transport and vertical structure of Asian dust from CALIPSO and surface measurements during PACDEX. J. Geophys. Res. Atmos. 113.

Hudson, E., Aihoshi, D., Gaines, T., Simard, G., Mullock, J., 2001. The Weather of Nunavut and the Arctic, Graphical Area Forecast 36 and 37. Nav Canada.
Jackson, C.I., 1965. The vertical profile of wind at Lake hazen, NWT. Arctic 18, 21–35.
Jackson, C.I., 1960. The Meteorology of Lake Hazen, Ellesmere Island, NWT. McGill University, Montreal.
Karanasiou, A., Moreno, N., Moreno, T., Viana, M., De Leeuw, F., Querol, X., 2012. Health effects from Sahara dust episodes in Europe: literature review and research gaps. Environ. Int. 47, 107–114.
Lehnherr, I., Louis, V.L.S., Sharp, M., Gardner, A.S., Smol, J.P., Schiff, S.L., Muir, D.C.G., Mortimer, C.A., Michelutti, N., Tarnocai, C., 2018. The world's largest High Arctic lake responds rapidly to climate warming. Nat. Commun. 9, 1–9.
Lohmann, U., Feichter, J., 2005. Global indirect aerosol effects: a review. Atmos. Chem. Phys. 5, 715–737.
Mei, L., Vandenbussche, S., Rozanov, V., Proestakis, E., Amiridis, V., Callewaert, S., Vountas, M., Burrows, J.P., 2020. On the retrieval of aerosol optical depth over cryosphere using passive remote sensing. Remote Sens. Environ. 241, 111731.
Mei, L., Xue, Y., de Leeuw, G., von Hoyningen-Huene, W., Kokhanovsky, A.A., Istomina, L., Guang, J., Burrows, J.P., 2013. Aerosol optical depth retrieval in the Arctic region using MODIS data over snow. Remote Sens. Environ. 128, 234–245.
Miller, S.D., Bankert, R.L., Solbrig, J.E., Forsythe, J.M., Noh, Y., Grasso, L.D., 2017. A dynamic enhancement with background reduction algorithm: overview and application to satellite-based dust storm detection. J. Geophys. Res. Atmos. 122, 12–938.
Nelson, D.L., Garay, M.J., Kahn, R.A., Dunst, B.A., 2013. Stereoscopic height and wind retrievals for aerosol plumes with the MISR INteractive eXplorer (MINX). Rem. Sens. 5, 4593–4628.
Neuman, C.M., 1990. Observations of winter aeolian transport and niveo-aeolian deposition at Crater Lake, Pangnirtung Pass, NWT, Canada. Permafr. Periglac. Process. 1, 235–247.
Painter, T.H., Bryant, A.C., Skiles, S.M., 2012. Radiative forcing by light absorbing impurities in snow from MODIS surface reflectance data. Geophys. Res. Lett. 39.
Peyridieu, S., Chédin, A., Capelle, V., Tsamalis, C., Pierangelo, C., Armante, R., Crevoisier, C., Crépeau, L., Siméon, M., Ducos, F., 2013. Characterisation of Dust Aerosols in the Infrared from IASI and Comparison with PARASOL, MODIS, MISR, CALIOP, and AERONET Observations.
Prospero, J.M., Bullard, J.E., Hodgkins, R., 2012. High-latitude dust over the North Atlantic: inputs from Icelandic proglacial dust storms. Science 84 335, 1078–1082.
Renfrew, I.A., Anderson, P.S., 2006. Profiles of katabatic flow in summer and winter over Coats Land, Antarctica. Q. J. R. Meteorol. Soc. A J. Atmos. Sci. Appl. Meteorol. Phys. Oceanogr. 132, 779–802.
Ritter, C., Notholt, J., Fischer, J., Rathke, C., 2005. Direct thermal radiative forcing of tropospheric aerosol in the Arctic measured by ground based infrared spectrometry. Geophys. Res. Lett. 32.
Schroth, A.W., Crusius, J., Gassó, S., Moy, C.M., Buck, N.J., Resing, J.A., Campbell, R.W., 2017. Atmospheric deposition of glacial iron in the Gulf of Alaska impacted by the position of the Aleutian Low. Geophys. Res. Lett. 44, 5053–5061.
Seidel, F.C., Rittger, K., Skiles, S.M., Molotch, N.P., Painter, T.H., 2016. Case study of spatial and temporal variability of snow cover, grain size, albedo and radiative forcing in the Sierra Nevada and Rocky Mountain snowpack derived from imaging spectroscopy. Cryosphere 10.
Shao, Y., Raupach, M.R., Findlater, P.A., 1993. Effect of saltation bombardment on the entrainment of dust by wind. J. Geophys. Res. Atmos. 98, 12719–12726.
St Pierre, K., 2018. Biogeochemical Impacts of Glacial Meltwaters across a High Arctic Watershed (Lake Hazen, Nunavut, Canada). University of Alberta.
Stephens, G.L., Vane, D.G., Tanelli, S., Im, E., Durden, S., Rokey, M., Reinke, D., Partain, P., Mace, G.G., Austin, R., 2008. CloudSat mission: performance and early science after the first year of operation. J. Geophys. Res. Atmos. 113.
Stout, J.E., 2001. Dust and environment in the southern high plains of North America. J. Arid Environ. 47, 425–441.
Tang, M., Cziczo, D.J., Grassian, V.H., 2016. Interactions of water with mineral dust aerosol: water adsorption, hygroscopicity, cloud condensation, and ice nucleation. Chem. Rev. 116, 4205–4259.
Vincent, R.F., 2018. The effect of Arctic dust on the retrieval of satellite derived sea and ice surface temperatures. Sci. Rep. 8, 1–10.
Washington, R., Todd, M.C., 2005. Atmospheric controls on mineral dust emission from the Bodélé Depression, Chad: the role of the low level jet. Geophys. Res. Lett. 32.
Whicker, J.J., Breshears, D.D., Wasiolek, P.T., Kirchner, T.B., Tavani, R.A., Schoep, D.A., Rodgers, J.C., 2002. Temporal and spatial variation of episodic wind erosion in unburned and burned semiarid shrubland. J. Environ. Qual. 31, 599–612.
Winker, D.M., Vaughan, M.A., Omar, A., Hu, Y., Powell, K.A., Liu, Z., Hunt, W.H., Young, S.A., 2009. Overview of the CALIPSO mission and CALIOP data processing algorithms. J. Atmos. Ocean. Technol. 26, 2310–2323.
Woo, M.K., Edlund, S.A., Young, K.L., 1991. Occurrence of early snow-free zones on Fosheim peninsula, Ellesmere Island, northwest territories. Curr. Res. Part B, Geol. Surv. Canada Pap. 91, 9–14.
Xie, Y., Zhang, W., Qu, J.J., 2017. Detection of asian dust storm using MODIS measurements. Rem. Sens. 9, 869.
Zwaaftink, C.D.G., Grythe, H., Skov, H., Stohl, A., 2016. Substantial contribution of northern high-latitude sources to mineral dust in the Arctic. J. Geophys. Res. Atmos. 121, 13–678.